Journal of Materials Chemistry A

PAPER

View Article Online
View Journal | View Issue

Open Access Article. Published on 12 mai 2015. Downloaded on 11.12.2025 07.52.12.
This article is licensed under a Creative Commons Attribution 3.0 Unported Licence.

Cite this: J. Mater. Chem. A, 2015, 3, 12958

# Oxygen storage capacity and thermal stability of the $CuMnO_2$–$CeO_2$ composite system†

Xiubing Huang, Chengsheng Ni, Guixia Zhao and John T. S. Irvine*

Received 19th February 2015
Accepted 12th May 2015

DOI: 10.1039/c5ta01361e

www.rsc.org/MaterialsA

Fast and reversible oxygen diffusion in solid oxides depending on oxygen partial pressure at low temperatures is a promising strategy for improving the overall performance and service lifetime of many energy-related materials. However, the high energy required for the redox reaction of cations and their high thermodynamic barriers have impeded the realization of fast oxygen diffusion at low temperatures. Herein, we report enhanced oxygen diffusion and storage capacity of monoclinic crednerite $CuMnO_2$ at a lower temperature by surface modification with $CeO_2$. The fast and reversible oxygen uptake/release can be attributed to $CeO_2$ that serves as a fast oxygen diffusion channel between bulk $CuMnO_2$ and the surrounding atmospheres. Importantly, the amount of $CeO_2$ in the $CuMnO_2$–$CeO_2$ composite system has a great effect on the total oxygen storage capacity and redox behaviour. Our findings could provide useful information for developing effective oxygen storage materials for wide energy-related applications.

## 1. Introduction

Solid-state oxygen storage materials (OSMs) have attracted considerable attention due to their wide applications in numerous oxygen-related energy and environmental fields, such as three-way catalysts for the effective removal of automobile exhaust emissions (*e.g.*, $NO_x$, CO, and hydrocarbons).[1,2] The development of OSMs is also crucial to the success of new energy technologies, such as oxygen enrichment to improve the efficiency of chemical looping combustion.[3] Ideal OSMs for practical applications should satisfy certain requirements and possess some properties, including large oxygen storage capacity (OSC), quick absorption/desorption of oxygen and their dependence on temperature and/or oxygen partial pressure, and good reversibility.

The most widely investigated OSMs are based on ceria (*e.g.*, well-known $Ce_{1-x}Zr_xO_{2+\delta}$) due to the reversible redox reaction of $Ce^{3+}/Ce^{4+}$,[2,4–8] however, their OSC is relatively small and usually achieved by the usage of reductive gas. Recently, oxides based on transition metals have attracted remarkable attention due to their excellent properties, such as their flexible oxidation states, various phase structures, possible substitutions, cationic and anionic non-stoichiometry, or lattice oxygen deficient in the framework.[3,9–13] Their oxygen storage/release behaviour is generally based on the oxygen non-stoichiometry, which can be achieved by adjusting the surrounding oxygen partial pressure (*i.e.*, oxidative air, reductive $H_2$) or temperature.[11,14] Among OSMs based on transition-metals, extensive attention has been paid to delafossite-type oxides with the general formula $CuMO_2$ (M = trivalent cation) because of the low reductive/oxidative temperature of $Cu^{2+}/Cu^{+}$, remarkable oxygen uptake ability, wide potential applications, environmental-friendliness and abundance.[15–17] However, only very limited work has been reported on the effect of trivalent cation species on the oxygen storage properties of the delafossite-type $CuMO_2$ oxides under oxidative/reductive atmospheres.[15–17] For example, Sumio Kato, *et al.* reported that $CuMnO_2$ and $CuFeO_2$ exhibited larger OSC values at lower temperature than those of $CuAlO_2$ and $CuGaO_2$,[15] and OSC values for $x = 0.1$ and 0.3 in $CuFe_{1-x}Al_xO_2$ were larger than that for $x = 0$ above 500 °C.[17] However, the full details of the phase-transformation process under oxidative/inert atmospheres and the effect of surface-modification by other metal oxides on the oxygen diffusion, oxygen storage capacity and thermal stability of $CuMO_2$ still remain not well-defined.

In the search for better OSMs, crednerite $CuMnO_2$ as an alternative phase to delafossite-type $CuMO_2$ seems to have great potential due to its changeable valence and low-temperature for oxygen uptake/release,[15,18] and its wide applications, such as a hydrogen photo-evolution catalyst,[19] a three-way catalyst for the removal of exhaust gases (*e.g.*, CO, $NO_x$),[15] and hydrogen storage.[20] As reported by several research groups, crednerite $CuMnO_2$ exhibits a monoclinic structure at room temperature, which consists of edge-shared $MnO_6$ octahedra and two-coordinated $Cu^{+}$ cations at the interlayer sites, as represented in Fig. 1.[15,19,21] This structure is closely related to the rhombohedral 3R delafossite structure of $CuFeO_2$ (*i.e.*, the $Cu^{+}$ cations linearly coordinating to two O ions, and the parallel O–Cu–O chains connecting $Fe^{3+}$ cations to form two-dimensional sheets

School of Chemistry, University of St Andrews, St Andrews, Fife, UK. E-mail: jtsi@st-andrews.ac.uk; Fax: +44 (0)1334463808; Tel: +44 (0)133463680

† Electronic supplementary information (ESI) available: Additional XRD, TGA/DTA, HRTEM and FESEM images as well as TEM elemental mappings. See DOI: 10.1039/c5ta01361e


This journal is © The Royal Society of Chemistry 2015

Open Access Article. Published on 12 mai 2015. Downloaded on 11.12.2025 07.52.12.
This article is licensed under a Creative Commons Attribution 3.0 Unported Licence.

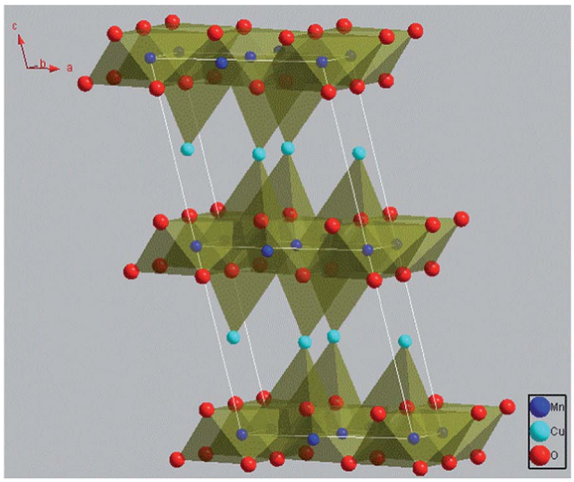


Fig. 1 Schematic illustration of the crystal structure of $CuMnO_2$. The illustration was drawn with Diamond 3.1d software for crystal and molecular structure visualization.

of edge-shared $FeO_6$ octahedra), but with a distortion of the $MnO_6$ octahedron due to the Jahn–Teller effect of $Mn^{3+}$.[22] However, it has been reported that $Cu_{1+x}Mn_{1-x}O_2$ ($0.08 < x < 0.12$) at high temperature can exhibit a delafossite-like phase with a hexagonal structure because the thermal expansion of the structure would result in a larger lattice distortion than that from the Jahn–Teller effect.[23,24]

It is well known that multiple valences of Mn cations can co-exist in many Mn-containing compounds, which could be beneficial to the oxygen-storage properties.[25–27] The valence of Mn in $CuMnO_2$ has been demonstrated to be +3, however the existence of $Mn^{4+}$ in the nonstoichiometric $Cu_{1+x}Mn_{1-x}O_2$ oxides is also detected by XPS because the excess Cu atoms would occupy the octahedral site with $Cu^{2+}$ while the electrical neutrality principle would result in the formation of mixed $Mn^{3+}/Mn^{4+}$.[18,28] In addition, the $Cu_xMn_{3-x}O_4$ spinel, one of the oxidation products of $CuMnO_2$, has been reported to show the coexistence of $Mn^{3+}/Mn^{4+}$, implying a possible increase in the total oxygen uptake ability under an oxidative atmosphere.[27,29,30] However, pure crednerite $CuMnO_2$ oxide is usually synthesized using the solid-state reaction at very high temperatures[15,31,32] or the ion-exchange reaction with a long reaction time.[32] Such a high reaction temperature or slow chemical conversion rate for reversible redox processes is impractical for many technological applications.[18] Therefore, it is important to improve the oxygen diffusion ability and the overall oxygen storage capacity of crednerite $CuMnO_2$ at low temperatures.

$CeO_2$ has been widely investigated as a three-way catalyst or an oxygen promoter due to the fast oxygen ionic mobility between $Ce^{4+}$ and $Ce^{3+}$ in a reductive/oxidative atmosphere even though $CeO_2$ could retain its fluorite structure under oxidizing and mildly reducing atmospheres.[33–37] $CeO_2$ has also been reported as an interlayer or electrolyte in the $La_{1-x}Sr_xCoO_{3-\delta}/CeO_2$ composite system to improve the oxygen ionic mobility, in which some chemical reactions can take place at the interfaces between perovskite and $CeO_2$.[38,39] Therefore, $CeO_2$ may function as an oxygen ionic mobility channel between oxides and their surrounding atmosphere. Here, we investigated the $CuMnO_2$–$CeO_2$ composite system with the purpose of further optimizing the oxygen diffusion ability and overall oxygen storage capacity at low temperatures under alternating oxidative (*i.e.*, air or $O_2$) and inert (*i.e.*, Ar) atmospheres. Modifying the surfaces of $CuMnO_2$ with $CeO_2$ may bring in both benefits of $CuMnO_2$ and $CeO_2$, thereafter adjusting their thermochemical properties (*e.g.*, redox properties, non-stoichiometry, oxygen exchange constant, and formation of oxygen vacancies), further enhancing their OSC and thermal stability. Our research results indicate that modifying $CuMnO_2$ with a small portion of $CeO_2$ (*e.g.*, the molar ratios of $CeO_2$ to $CuMnO_2$ smaller than 20%) can improve the oxygen storage capacity at low temperatures (<600 °C) in a highly reversible manner.

## 2. Experimental section

### 2.1 Sample preparation

$CuMnO_2$–$CeO_2$ composites were prepared by a conventional Pechini method, followed by a solid state method. In a typical process, 10 mmol of $Cu(NO_3)_2\cdot 2.5H_2O$ (98%) and 10 mmol of $Mn(CH_3COO)_2\cdot 4H_2O$ (98%) were dissolved in 100 mL of deionized $H_2O$ under continuous stirring. A certain amount (0.5, 1.0, 2.0 or 4.0 mmol) of $Ce(NO_3)_3\cdot 6H_2O$ (99.99%) was added into the above solution under stirring, followed by adding 20 mmol of citric acid monohydrate (99.95%) and 10 mL of ethylene glycol. After stirring for 4 h, the solvent was evaporated at 110 °C to obtain a gel. After drying, the powder was ground and pre-fired at 500 °C under static air for 1 h to obtain the precursor, then the precursor was pressed into pellets and fired at 960 °C for 12 h under flowing argon. The obtained products were referred to as $CuMnO_2$–$x$$CeO_2$, in which $x$ is the molar ratio percent of $CeO_2$ to $CuMnO_2$ (*i.e.*, $x$ = mol of $CeO_2$/mol of $CuMnO_2 \times 100$).

### 2.2 Characterization

Structures of all samples were characterized by X-ray powder diffraction (XRD) on a PANalytical Empyrean Reflection Diffractometer with Cu Kα irradiation ($\lambda$ = 0.15418 nm). HRTEM images and TEM elemental mapping of samples were observed on a JEM-2011 Transmission Electron Microscope (TEM) with an acceleration voltage of 200 kV equipped with an X-ray Energy Dispersive spectrometer (EDS). The morphologies of all samples were observed on a JEOL JSM-6700 Field Scanning Electron Microscope (FESEM). The oxygen uptake behaviours of these samples were measured by thermogravimetric analysis (TGA) on a NETZSCH TG 209 instrument (NETZSCH-Geraetebau GmbH, Selb, Germany) with a TASC 414/3 controller. The measurements were carried out for 50 mg specimens up to 800 °C with a heating rate of 10 °C $min^{-1}$ under air or $O_2$ with flowing rate 25 mL $min^{-1}$. In addition, the reversibility of the oxygen uptake/release was carried out in the following experiments: first increasing the temperature to 600 °C under flowing $O_2$ gas, then switching the gas from $O_2$ to Ar with temperature from 600 to 900 °C; after cooling down to 300 °C under flowing Ar, switching the gas from Ar to $O_2$ with temperature from 300

Open Access Article. Published on 12 mai 2015. Downloaded on 11.12.2025 07.52.12.
This article is licensed under a Creative Commons Attribution 3.0 Unported Licence.

to 600 °C; this process was repeated between 300 and 900 °C 4 times. The thermal stability (weight and phase structural changes) of the as-prepared samples with temperature from room temperature to 1000 °C under flowing air was checked using a TGA/DTA technique carried out on a Stanton Redcroft STA-780 series thermal analyser.

## 3. Results and discussion

XRD patterns of these as-prepared $CuMnO_2$–$xCeO_2$ composites obtained by post-annealing at 960 °C for 12 h under flowing Ar are shown in Fig. 2. The XRD pattern for $CuMnO_2$ in Fig. 2a can be indexed to a pure monoclinic structure with a $C2/m$ space group. All the peaks are in good agreement with the JCPDS card no. 50-0860 for the crednerite phase. For the $CuMnO_2$–$xCeO_2$ composites, they are obviously composed of crednerite $CuMnO_2$ and fluorite $CeO_2$, and no other impurity phases are observed. The XRD Rietveld refinements for $CuMnO_2$ and $CeO_2$ were carried out using GSAS software based on the monoclinic structure with the $C2/m$ space group and cubic structure with the $Fm\bar{3}m$ space group, respectively. The typical XRD patterns after final refinement for $CuMnO_2$ and $CuMnO_2$–$40CeO_2$ are shown in Fig. 3, further confirming the phase composition of $CuMnO_2$ and $CeO_2$.[21]

Detailed lattice parameters for pure $CuMnO_2$ and $CuMnO_2$–$xCeO_2$ composites after Rietveld refinements are summarized in Table 1. There are no obvious changes in the lattice parameters $a$, $b$ and $c$ for $CuMnO_2$ and $a$ for $CeO_2$ with the increasing $CeO_2$ amount up to $x = 40$ for the $CuMnO_2$–$xCeO_2$ composite, suggesting that $CuMnO_2$ and $CeO_2$ exist mainly as separate phases and there may be only a little contact between the surfaces. The HRTEM images of $CuMnO_2$ in $CuMnO_2$–$10CeO_2$ and $CuMnO_2$–$40CeO_2$ (Fig. S1†) show clear lattice fringes and these $d$ spacings of 0.22 and 0.57 nm correspond to the (111) and (001) planes of $CuMnO_2$, respectively.

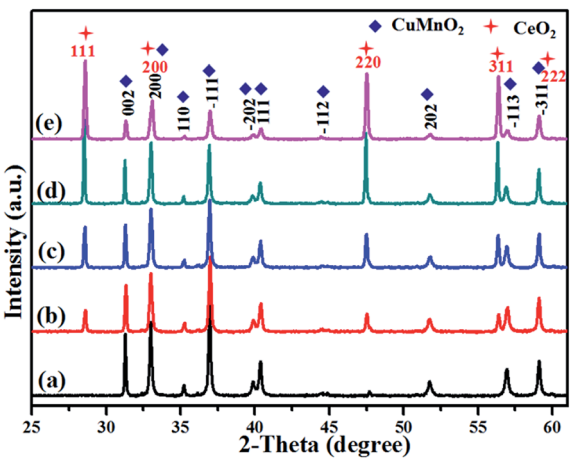


Fig. 2 XRD patterns of the as-prepared $CuMnO_2$–$xCeO_2$ (*i.e.*, post-annealed at 960 °C under flowing Ar): (a) $CuMnO_2$, (b) $CuMnO_2$–$5CeO_2$, (c) $CuMnO_2$–$10CeO_2$, (d) $CuMnO_2$–$20CeO_2$, and (e) $CuMnO_2$–$40CeO_2$.

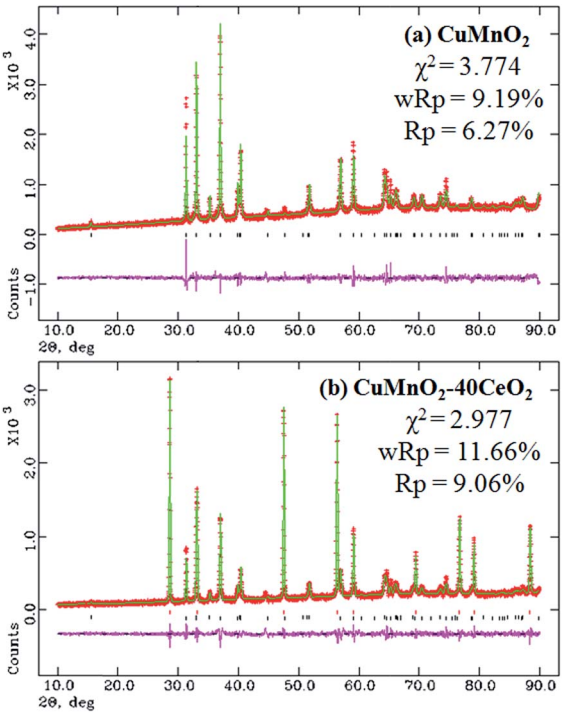


Fig. 3 XRD patterns after final Rietveld refinements for the as-prepared products: (a) $CuMnO_2$ and (b) $CuMnO_2$–$40CeO_2$.

The TEM elemental mappings of Cu, Mn, O and Ce for $CuMnO_2$–$10CeO_2$ (Fig. S2†) and $CuMnO_2$–$40CeO_2$ (Fig. S3†) also indicate the individual existence of $CuMnO_2$ and $CeO_2$, as well as the inhomogeneous surface contact between $CeO_2$ and $CuMnO_2$.

The oxygen uptake behaviours of the as-prepared $CuMnO_2$–$xCeO_2$ composites were investigated by TGA at temperature up to 800 °C under flowing air or $O_2$. The results shown in Fig. 4 reveal a remarkable oxygen uptake capacity of this $CuMnO_2$–$xCeO_2$ composite system under an oxidative atmosphere, which corresponds to the following exothermic oxidation reaction:

$$CuMnO_2 + 1/(6 - 2y)O_2 \rightarrow 1/(3 - y)Cu_yMn_{3-y}O_4 + (3 - 2y)/(3 - y)CuO \quad (1)$$

The weight for all these samples starts to increase at about 300 °C, due to the increase in the oxygen content, accompanied by the oxidation of $Cu^+$ and/or $Mn^{3+}$. Pure $CuMnO_2$ had a continuous and smooth weight increase with increasing temperature from 300 to 800 °C, reaching the maximum value of 5.475 wt% at 800 °C under both flowing air and $O_2$, corresponding to the formation of spinel $Cu_{1.058}Mn_{1.942}O_4$. For pure $CuMnO_2$ and $CuMnO_2$–$xCeO_2$ composites, the oxygen uptake rate in air is a bit slower than that in $O_2$ and the maximum oxygen uptake amount in air is also a bit smaller than that in $O_2$, in which $CuMnO_2$–$5CeO_2$ exhibits the most weight increase, reaching 6.169 wt% at 591 °C under flowing $O_2$ and 6.031 wt% at 620 °C under flowing air, respectively, suggesting that higher oxygen partial pressure would enhance the oxygen uptake

 This journal is © The Royal Society of Chemistry 2015

Open Access Article. Published on 12 mai 2015. Downloaded on 11.12.2025 07.52.12.
This article is licensed under a Creative Commons Attribution 3.0 Unported Licence.

Table 1 Lattice parameters of the as-prepared $CuMnO_2$–$xCeO_2$ obtained from Rietveld refinements using GSAS software

| As-prepared sample | Composition | $a$ (Å) | $b$ (Å) | $c$ (Å) | Cell volume (Å$^3$) | $\beta$ |
|---|---|---|---|---|---|---|
| $CuMnO_2$ | $CuMnO_2$ | 5.592(3) | 2.883(1) | 5.892(3) | 92.1(1) | 104.03(3) |
| $CuMnO_2$–$5CeO_2$ | $CuMnO_2$ | 5.597(3) | 2.883(1) | 5.892(3) | 92.2(1) | 104.00(4) |
| | $CeO_2$ | | 5.412(2) | | 158.5(2) | |
| $CuMnO_2$–$10CeO_2$ | $CuMnO_2$ | 5.593(1) | 2.883(6) | 5.892(1) | 92.19(3) | 104.06(3) |
| | $CeO_2$ | | 5.412(1) | | 158.5(2) | |
| $CuMnO_2$–$20CeO_2$ | $CuMnO_2$ | 5.589(2) | 2.882(1) | 5.891(2) | 92.08(8) | 104.08(4) |
| | $CeO_2$ | | 5.411(1) | | 158.4(1) | |
| $CuMnO_2$–$40CeO_2$ | $CuMnO_2$ | 5.597(3) | 2.883(1) | 5.891(3) | 92.24(9) | 104.06(7) |
| | $CeO_2$ | | 5.412(2) | | 158.5(3) | |

ability at lower temperatures. With the further increase of $CeO_2$ amount in the composite, the maximum OSC decreased, which can be attributed to the offset effect of $CeO_2$ since the weight increase is mainly caused by the oxidation of $Cu^+$ and/or $Mn^{3+}$ in $CuMnO_2$ while $CeO_2$ could maintain its fluorite-type structure under an inert atmosphere,[40,41] as determined by the XRD results in Fig. 2. After reaching the maximum weight at around 600 °C, further increasing the temperature to 800 °C results in a slight and smooth weight decrease (<0.14 wt%) for all these $CeO_2$-modified $CuMnO_2$ samples, which can be attributed to the composition adjustment of spinel $Cu_yMn_{3-y}O_4$ with temperature.[18] These results also indicate that $CeO_2$-modification would favour the oxygen mobility in $CuMnO_2$ and the formation of spinel $Cu_yMn_{3-y}O_4$ with more $Mn^{4+}$ at lower temperatures. It should be noted that the oxygen uptake in $CuMnO_2$ and $CuMnO_2$–$xCeO_2$ composites mainly comes from the oxidation of $CuMnO_2$ to CuO and spinel $Cu_yMn_{3-y}O_4$. Assuming that the total weight increase only comes from the oxidation of $CuMnO_2$, the composition of spinel $Cu_yMn_{3-y}O_4$ at the maximum weight under flowing $O_2$ can be calculated based on eqn (1) to be $Cu_{1.370}Mn_{1.630}O_4$ for the $CuMnO_2$–$5CeO_2$ starting mix, $Cu_{1.317}Mn_{1.683}O_4$ for $CuMnO_2$–$10CeO_2$, $Cu_{1.356}Mn_{1.644}O_4$ for $CuMnO_2$–$20CeO_2$ and $Cu_{1.316}Mn_{1.684}O_4$ for $CuMnO_2$–$40CeO_2$, while the composition of spinels at the maximum weight under flowing air can be calculated to be $Cu_{1.332}Mn_{1.668}O_4$ for $CuMnO_2$–$5CeO_2$, $Cu_{1.296}Mn_{1.704}O_4$ for $CuMnO_2$–$10CeO_2$, $Cu_{1.310}Mn_{1.690}O_4$ for $CuMnO_2$–$20CeO_2$ and $Cu_{1.268}Mn_{1.732}O_4$ for $CuMnO_2$–$40CeO_2$, respectively. These calculation results suggest that higher oxygen partial pressure favours the formation of spinels with more $Mn^{4+}$ from the oxidation of $CuMnO_2$–$xCeO_2$ composites.

XRD patterns of the oxygenated $CuMnO_2$ and $CuMnO_2$–$xCeO_2$ composites after the TGA test up to 800 °C under flowing air are shown in Fig. 5. While $CeO_2$ in these oxygenated $CuMnO_2$–$xCeO_2$ composites still maintained its fluorite-type cubic structure, $CuMnO_2$ was oxidized to CuO and spinel $Cu_yMn_{3-y}O_4$ oxides, in good agreement with the TGA analysis in Fig. 4 and previous reported results.[18] The lattice parameters of $CeO_2$ and spinel $Cu_yMn_{3-y}O_4$ in the oxygenated $CuMnO_2$ and $CuMnO_2$–$xCeO_2$ composites after the TGA test up to 800 °C in flowing air were refined from the XRD results in Fig. 5 using GSAS software and are summarized in Table 2. The lattice parameters of $CeO_2$ in the oxygenated $CuMnO_2$–$xCeO_2$ composites are a bit smaller than those of the as-prepared $CuMnO_2$–$xCeO_2$ composites (as shown in Table 1), indicating the possible doping of Mn and/or Cu in the lattice of $CeO_2$ after oxidation. In addition, the lattice parameters of spinel $Cu_yMn_{3-y}O_4$ in the oxygenated $CuMnO_2$–$xCeO_2$ composites are also slightly smaller than those of oxygenated pure $CuMnO_2$,

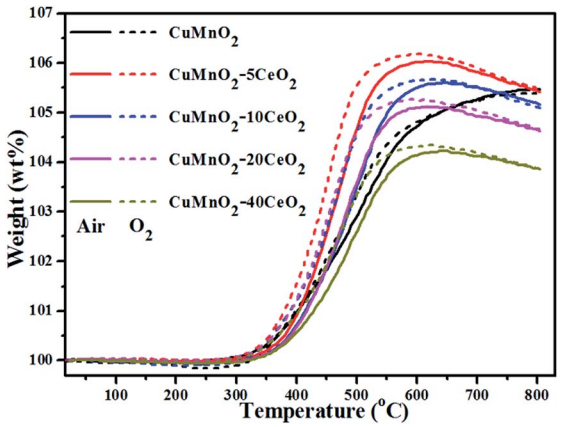


Fig. 4 TGA curves of the as-prepared $CuMnO_2$–$xCeO_2$ samples (*i.e.*, post-annealed at 960 °C under flowing Ar for 12 h) under flowing air or pure $O_2$ with 25 mL min$^{-1}$ from room temperature to 800 °C. The solid lines are the TGA curves under air and the short dashed lines are the TGA curves under pure $O_2$.

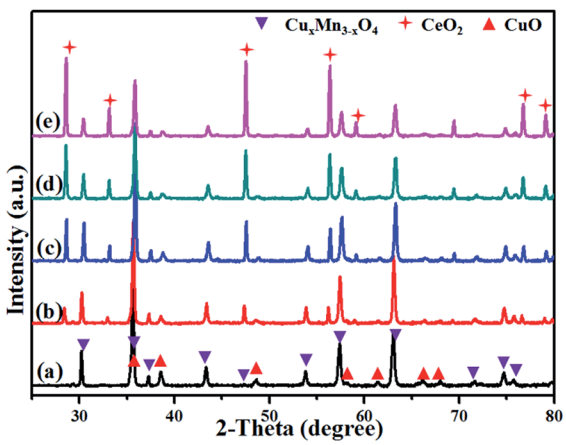


Fig. 5 XRD patterns after the TGA test from room temperature to 800 °C under flowing air: (a) $CuMnO_2$, (b) $CuMnO_2$–$5CeO_2$, (c) $CuMnO_2$–$10CeO_2$, (d) $CuMnO_2$–$20CeO_2$, and (e) $CuMnO_2$–$40CeO_2$.

Open Access Article. Published on 12 mai 2015. Downloaded on 11.12.2025 07.52.12.
This article is licensed under a Creative Commons Attribution 3.0 Unported Licence.

Table 2 Lattice parameters of oxygenated $CuMnO_2$–$xCeO_2$ in Fig. 5 from Rietveld refinements using GSAS software

| Oxygenated $CuMnO_2$–$xCeO_2$ | Composition | $a$ (Å) | Cell volume (Å$^3$) |
|---|---|---|---|
| $CuMnO_2$ | $Cu_yMn_{3-y}O_4$ | 8.317(2) | 575.30(7) |
| $CuMnO_2$–$5CeO_2$ | $Cu_yMn_{3-y}O_4$ | 8.307(2) | 573.23(4) |
| | $CeO_2$ | 5.407(8) | 158.14(7) |
| $CuMnO_2$–$10CeO_2$ | $Cu_yMn_{3-y}O_4$ | 8.311(5) | 574.06(3) |
| | $CeO_2$ | 5.409(1) | 158.26(1) |
| $CuMnO_2$–$20CeO_2$ | $Cu_yMn_{3-y}O_4$ | 8.309(4) | 573.64(9) |
| | $CeO_2$ | 5.410(6) | 158.39(3) |
| $CuMnO_2$–$40CeO_2$ | $Cu_yMn_{3-y}O_4$ | 8.312(2) | 574.27(1) |
| | $CeO_2$ | 5.410(2) | 158.35(8) |

indicating the higher Cu/Mn ratios in the spinel $Cu_yMn_{3-y}O_4$ in the oxygenated $CuMnO_2$–$xCeO_2$ composites as the smaller ionic radii of $Cu^{2+}$ than that of $Mn^{2+}$ would result in a decrease of lattice parameters when copper ions replace manganese ions on tetrahedral sites.

To further check their thermal stability with temperature under flowing air, we treated the as-prepared samples (*i.e.*, post-annealed at 960 °C for 12 h under flowing Ar) from room temperature up to 1000 °C with heating and cooling rates of ±10 °C min$^{-1}$ under flowing air, as shown in Fig. 6. As discussed in aforementioned paragraphs, the as-prepared samples can start to take up oxygen near 300 °C and reach the maximum values at near 600 °C for $CuMnO_2$–$xCeO_2$ composites and 800 °C for pure $CuMnO_2$, respectively. On further heating, these samples exhibit a steep weight loss from 960 °C accompanied by an endothermic peak in the DTA curves, as shown in Fig. S4.† Such behaviour can be attributed to the transformation of spinels and CuO back into a crednerite $Cu_{1+y'}Mn_{1-y'}O_2$ phase, accompanied by the release of $O_2$.[18,32] During the cooling process under flowing air from 1000 °C, there is a sharp continuous weight increase up to around 880 °C, which can be attributed to the re-oxidation of the crednerite phase to CuO and spinel oxides. The slight weight increase from 880 to 600 °C can be attributed to the composition adjustment of spinels with the cooling temperature, as determined by XRD shown in Fig. S5.† Notably, their weights at 1000 °C are higher than their pristine counterparts, suggesting that CuO and spinel $Cu_yMn_{3-y}O_4$ at high temperature under air can be converted to $Cu_{1+y'}Mn_{1-y'}O_2$ rather than $CuMnO_2$ according to eqn (2).

$$1/(3-y)Cu_yMn_{3-y}O_4 + (3-2y)/(3-y)CuO \rightarrow \alpha Cu_{x'}Mn_{3-x'}O_4 + (2-\alpha)/2Cu_{1+y'}Mn_{1-y'}O_2 + [1/(6-2y) - \alpha/2]O_2 \quad (2)$$

where $\alpha = 2y'/(3 + 3y' - 2x')$.

The TGA behaviours of the oxygenated $CuMnO_2$–$xCeO_2$ composites (*i.e.*, after the TGA test up to 800 °C under flowing $O_2$) with temperature up to 900 °C under flowing argon are displayed in Fig. 7. The results show that all these samples are stable up to around 600 °C under flowing argon. Further increasing temperature would lead to a continuous weight loss (<1.2 wt%) up to about 790 °C, in which the oxygenated $CuMnO_2$–$5CeO_2$ exhibited the most weight loss and the total weight loss decreased with the increase of $CeO_2$. The small weight loss can be attributed to the removal of oxygen in spinels. At temperatures higher than 790 °C, these sharp weight losses are attributed to the further removal of oxygen to form crednerite $Cu_{1+y'}Mn_{1-y'}O_2$.[31] To further support this conclusion, we treated the oxygenated $CuMnO_2$, $CuMnO_2$–$5CeO_2$ and $CuMnO_2$–$20CeO_2$ under flowing argon at 900 °C for 2 h and their XRD patterns shown in Fig. S6† indicate the reformation of the crednerite $CuMnO_2$ structure. The total weight losses for the oxygenated $CuMnO_2$–$5CeO_2$, $CuMnO_2$–$10CeO_2$ and $CuMnO_2$–$20CeO_2$ are higher than that for oxygenated $CuMnO_2$. The enhanced oxygen mobility and storage capacity of the $CuMnO_2$–$xCeO_2$ composite system can be attributed to the synergistic effect between $CuMnO_2$ and $CeO_2$, in which $CeO_2$ can act as an oxygen transfer channel or oxygen promoter dependent on temperature and/or oxygen partial pressures. The possible doping or exsolution of Cu/Mn into or from the lattice of $CeO_2$ on the surface depending on the temperature and oxygen partial pressure may also contribute to the enhanced

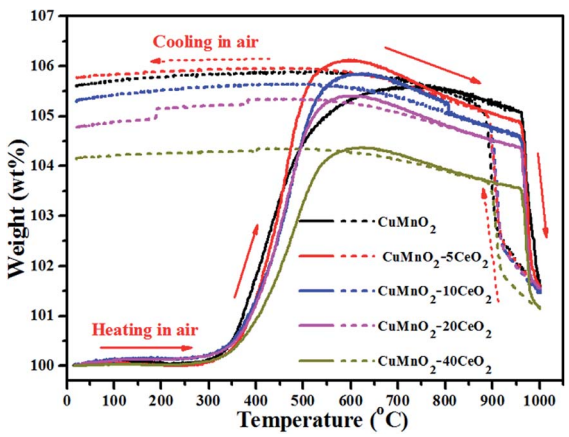


Fig. 6 TGA curves of the as-prepared $CuMnO_2$–$xCeO_2$ samples (*i.e.*, post-annealed at 960 °C for 12 h under flowing Ar) from room temperature up to 1000 °C with heating and cooling rates of 10 °C min$^{-1}$ under flowing air.

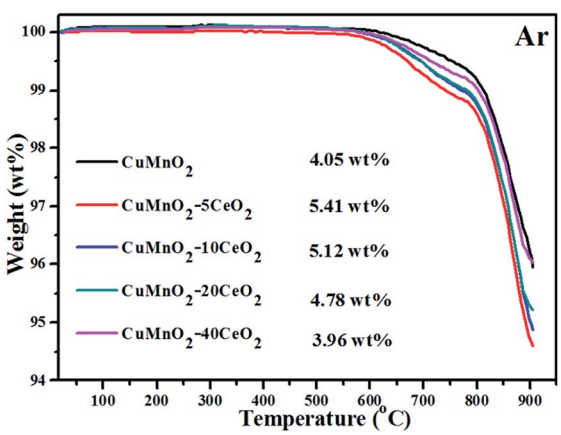


Fig. 7 TGA curves of oxidized $CuMnO_2$–$xCeO_2$ samples (*i.e.*, after the TGA test up to 800 °C under flowing $O_2$) from room temperature to 900 °C under flowing argon with 25 mL min$^{-1}$.


This journal is © The Royal Society of Chemistry 2015

Open Access Article. Published on 12 mai 2015. Downloaded on 11.12.2025 07.52.12.
This article is licensed under a Creative Commons Attribution 3.0 Unported Licence.

performance. Therefore, with the surface modification of $CeO_2$, $CuMnO_2$ can take up oxygen from $CeO_2$ rather than directly from the surrounding $O_2$ atmosphere and *vice versa*, under an inert Ar atmosphere, CuO and spinel $Cu_yMn_{3-y}O_4$ can release oxygen to the $CeO_2$ lattice and then to the surroundings, rather than directly to the surroundings.

From the TGA data in Fig. 4, it appears that these $CeO_2$-modified $CuMnO_2$ oxides can be oxidized from 300 °C and reach the maximum weight at around 600 °C under flowing $O_2$, while the oxygenated samples can start to release oxygen from 600 °C under flowing argon based on the TGA results in Fig. 7. These results indicate that $CeO_2$-modified $CuMnO_2$ oxides can cause either oxygen uptake or release depending on the temperature and/or oxygen partial pressure. Thus, remarkable oxygen uptake/release behaviours are expected *via* adjusting the temperature and oxygen partial pressure. As demonstrated in Fig. 8, $CuMnO_2$ and $CeO_2$-modified $CuMnO_2$ oxides can take up/release a large amount of oxygen in which $CuMnO_2$–$5CeO_2$ exhibits the highest OSC (*ca.* 6.0 wt%) and $CuMnO_2$–$20CeO_2$ shows the best reversibility under the alternating $O_2$ and argon between 300 and 900 °C for four cycles, indicating that $CeO_2$ modification would improve the oxygen storage capacity as well as the reversibility of $CuMnO_2$. The OSC and reversibility would become worse with the increasing cycle times, as shown in Fig. S7,† but the final weight after each treatment under flowing argon during the cycles almost remains the same, indicating that the gradual weight loss may be due to the formation of spinels with less $Mn^{4+}$ during the oxidation process with the increasing cycling times. As shown in Fig. S8,† after a nine cycle test under alternating $O_2$ and argon, $CuMnO_2$–$5CeO_2$ still contains crednerite $CuMnO_2$ and fluorite $CeO_2$ phases; however, there are obvious $CeO_2$ nanoparticles on the $CuMnO_2$ surface, in comparison to the FESEM images in Fig. S9.† The TEM results for $CuMnO_2$–$10CeO_2$ after the TGA test, as shown in Fig. S10,† also indicate the appearance of $CeO_2$ nanoparticles on the surface of $CuMnO_2$, which resulted in a worse performance for the oxidation of $CuMnO_2$. The TEM elemental mapping results for $CuMnO_2$–$10CeO_2$ in Fig. S10† suggest that some Cu is doped into the lattice of $CeO_2$ while Mn is still in $CuMnO_2$, which can be explained by the bigger ionic radius of $Cu^{2+}$ (0.73 Å) and $Cu^{+}$ (0.77 Å) than that of $Mn^{3+}$ (0.58 Å) and $Mn^{4+}$ (0.53 Å).

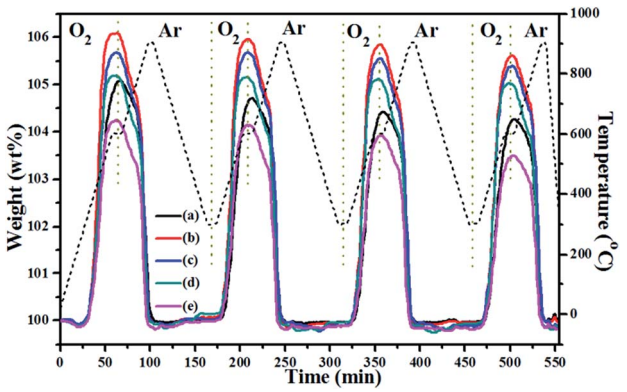


Fig. 8 TGA curves of the as-prepared $CuMnO_2$–$xCeO_2$ samples (*i.e.*, post-annealed at 960 °C for 12 h under flowing Ar) under alternating $O_2$ and argon. The samples were first oxidized under $O_2$ to 600 °C, then the gas was switched to argon and the temperature was increased to 900 °C. After being cooled down to 300 °C under argon, the gas was then switched back to $O_2$ and oxidized to 600 °C.

## 4. Conclusions

In conclusion, we found that fast and reversible oxygen mobility, and increased oxygen storage capacity of crednerite $CuMnO_2$ could be achieved at reduced temperatures (*ca.* 600 °C) by surface modification with $CeO_2$ at an amount less than 20 mol% in the $CuMnO_2$–$CeO_2$ composite system. The fast and reversible oxygen uptake/release and increased oxygen storage capacity at lower temperatures can be attributed to the synergistic effect of $CeO_2$ as an oxygen diffusion channel between bulk $CuMnO_2$ and the surrounding atmospheres, favouring the reversible formation of spinels at lower temperatures. Our findings reported here could provide a pathway for the design and development of effective oxygen storage materials for a range of energy-synergetic related applications at low temperatures.

## Acknowledgements

The authors gratefully thank the Engineering and Physical Sciences Research Council (EPSRC) platform grant EP/I022570/1 and EP/I022570/2 for financial support.

## Notes and references

1 H. C. Yao and Y. F. Y. Yao, *J. Catal.*, 1984, **86**, 254–265.
2 C. E. Hori, H. Permana, K. Y. S. Ng, A. Brenner, K. More, K. M. Rahmoeller and D. Belton, *Appl. Catal., B*, 1998, **16**, 105–117.
3 T. Motohashi, Y. Hirano, Y. Masubuchi, K. Oshima, T. Setoyama and S. Kikkawa, *Chem. Mater.*, 2013, **25**, 372–377.
4 M. Ozawa, M. Kimura and A. Isogai, *J. Alloys Compd.*, 1993, **193**, 73–75.
5 A. Gupta, U. V. Waghmare and M. S. Hegde, *Chem. Mater.*, 2010, **22**, 5184–5198.
6 M. P. Yeste, J. C. Hernandez-Garrido, D. C. Arias, G. Blanco, J. M. Rodriguez-Izquierdo, J. M. Pintado, S. Bernal, J. A. Perez-Omil and J. J. Calvino, *J. Mater. Chem. A*, 2013, **1**, 4836–4844.
7 X. Wang, G. Lu, Y. Guo, L. Jiang, Y. Guo and C. Li, *J. Mater. Sci.*, 2009, **44**, 1294–1301.
8 Q. Dong, S. Yin, C. Guo, T. Kimura and T. Sato, *RSC Adv.*, 2012, **2**, 12770–12774.
9 S. Remsen and B. Dabrowski, *Chem. Mater.*, 2011, **23**, 3818–3827.
10 O. Parkkima, H. Yamauchi and M. Karppinen, *Chem. Mater.*, 2013, **25**, 599–604.
11 S. Carter, A. Selcuk, R. J. Chater, J. Kajda, J. A. Kilner and B. C. H. Steele, *Solid State Ionics*, 1992, **53–56**, 597–605.

Open Access Article. Published on 11.12.2025 07.52.12.
This article is licensed under a Creative Commons Attribution 3.0 Unported Licence.

12 M. Cherry, M. S. Islam and C. R. A. Catlow, *J. Solid State Chem.*, 1995, **118**, 125–132.
13 J. W. Lekse, S. Natesakhawat, D. Alfonso and C. Matranga, *J. Mater. Chem. A*, 2014, **2**, 2397–2404.
14 H. Jeen, W. S. Choi, M. D. Biegalski, C. M. Folkman, I. C. Tung, D. D. Fong, J. W. Freeland, D. Shin, H. Ohta, M. F. Chisholm and H. N. Lee, *Nat. Mater.*, 2013, **12**, 1057–1063.
15 S. Kato, R. Fujimaki, M. Ogasawara, T. Wakabayashi, Y. Nakahara and S. Nakata, *Appl. Catal., B*, 2009, **89**, 183–188.
16 S. Kato, H. Sato, M. Ogasawara, T. Wakabayashi, Y. Nakahara and S. Nakata, *Solid State Sci.*, 2012, **14**, 177–181.
17 S. Kato, S. Suzuki, R. Kawashima, M. Ogasawara, T. Wakabayashi, Y. Nakahara and S. Nakata, *J. Mater. Sci.*, 2013, **48**, 8077–8083.
18 M. Trari, J. Töpfer, P. Dordor, J. C. Grenier, M. Pouchard and J. P. Doumerc, *J. Solid State Chem.*, 2005, **178**, 2751–2758.
19 Y. Bessekhouad, M. Trari and J. P. Doumerc, *Int. J. Hydrogen Energy*, 2003, **28**, 43–48.
20 S. A. M. Abdel-Hameed, F. H. Margha and A. A. El-Meligi, *Int. J. Energy Res.*, 2014, **38**, 459–465.
21 Y. Bessekhouad, Y. Gabes, A. Bouguelia and M. Trari, *J. Mater. Sci.*, 2007, **42**, 6469–6476.
22 J. Topfer, M. Trari, P. Gravereau, J. P. Chaminade and J. P. Doumerc, *Z. Kristallogr.*, 1995, **210**, 184–187.
23 F. C. M. Driessens and G. D. Rieck, *Z. Anorg. Allg. Chem.*, 1967, **351**, 48–62.
24 P. Wei, M. Bieringer, L. D. Cranswick and A. Petric, *J. Mater. Sci.*, 2010, **45**, 1056–1064.
25 J. Li, S. Xiong, X. Li and Y. Qian, *Nanoscale*, 2013, **5**, 2045–2054.
26 N. K. Radhakrishnan and A. B. Biswas, *Phys. Status Solidi A*, 1977, **44**, 45–49.
27 D. P. Shoemaker, J. Li and R. Seshadri, *J. Am. Chem. Soc.*, 2009, **131**, 11450–11457.
28 H. Y. Chen and D. J. Hsu, *J. Alloys Compd.*, 2014, **598**, 23–26.
29 I. N. Dubrovina, V. F. Balakirev and A. V. Antonov, *Inorg. Mater.*, 2001, **37**, 76–81.
30 E. Ríos, S. Abarca, P. Daccarett, H. Nguyen Cong, D. Martel, J. F. Marco, J. R. Gancedo and J. L. Gautier, *Int. J. Hydrogen Energy*, 2008, **33**, 4945–4954.
31 A. P. Amrute, Z. Łodziana, C. Mondelli, F. Krumeich and J. Pérez-Ramírez, *Chem. Mater.*, 2013, **25**, 4423–4435.
32 B. Bellal, B. Hadjarab, N. Benreguia, Y. Bessekhouad and M. Trari, *J. Appl. Electrochem.*, 2011, **41**, 867–872.
33 Z. Liu, Z. Wu, X. Peng, A. Binder, S. Chai and S. Dai, *J. Phys. Chem. C*, 2014, **118**, 27870–27877.
34 L. Shi, W. Chu, F. Qu and S. Luo, *Catal. Lett.*, 2007, **113**, 59–64.
35 A. Hornés, A. B. Hungría, P. Bera, A. L. Cámara, M. Fernández-García, A. Martínez-Arias, L. Barrio, M. Estrella, G. Zhou, J. J. Fonseca, J. C. Hanson and J. A. Rodriguez, *J. Am. Chem. Soc.*, 2009, **132**, 34–35.
36 S. D. Senanayake, D. Stacchiola and J. A. Rodriguez, *Acc. Chem. Res.*, 2013, **46**, 1702–1711.
37 I. Moog, C. Feral-Martin, M. Duttine, A. Wattiaux, C. Prestipino, S. Figueroa, J. Majimel and A. Demourgues, *J. Mater. Chem. A*, 2014, **2**, 20402–20414.
38 E. Y. Konysheva, S. M. Francis, J. T. S. Irvine, A. Rolle and R.-N. Vannier, *J. Mater. Chem.*, 2011, **21**, 15511–15520.
39 E. Konysheva, R. Blackley and J. T. S. Irvine, *Chem. Mater.*, 2010, **22**, 4700–4711.
40 A. S. Ivanova, *Kinet. Catal.*, 2009, **50**, 797–815.
41 Y. Zhou and M. N. Rahaman, *Acta Mater.*, 1997, **45**, 3635–3639.


This journal is © The Royal Society of Chemistry 2015